



Article

# Multi-Domain Data Integration for Plasma Diagnostics in Semiconductor Manufacturing Using Tri-CycleGAN

Minji Kang <sup>1,2,†</sup>, Sung Kyu Jang <sup>3,†</sup> , Jihun Kim <sup>3</sup>, Seongho Kim <sup>1,2</sup>, Changmin Kim <sup>4</sup>, Hyo-Chang Lee <sup>5</sup>,  
Wooseok Kang <sup>1,6</sup>, Min Sup Choi <sup>2</sup>, Hyeongkeun Kim <sup>3,\*</sup> and Hyeong-U Kim <sup>1,7,\*</sup> 

- <sup>1</sup> Semiconductor Manufacturing Research Center, Korea Institute of Machinery and Materials (KIMM), Daejeon 34103, Republic of Korea; kmj0302@kimm.re.kr (M.K.); kimho6344@kimm.re.kr (S.K.); kang@kimm.re.kr (W.K.)
  - <sup>2</sup> Department of Materials Science and Engineering, Chungnam National University (CNU), Daejeon 34134, Republic of Korea; goodcms@cnu.ac.kr
  - <sup>3</sup> Electronic Convergence Material and Device Research Center, Korea Electronics Technology Institute (KETI), Seongnam 13509, Republic of Korea; skjang@keti.re.kr (S.K.J.); kjh96@keti.re.kr (J.K.)
  - <sup>4</sup> Memory Etch Technology Team, Samsung Electronics, Pyeongtaek 17786, Republic of Korea; cm3.kim@samsung.com
  - <sup>5</sup> School of Electronics and Computer Engineering, Korea Aerospace University (KAU), Goyang 10540, Republic of Korea; plasma@kau.ac.kr
  - <sup>6</sup> Mechanical Engineering, KIMM Campus, University of Science & Technology (UST), Daejeon 34113, Republic of Korea
  - <sup>7</sup> Nano-Mechatronics, KIMM Campus, University of Science & Technology (UST), Daejeon 34113, Republic of Korea
- \* Correspondence: faithkim99@keti.re.kr (H.K.); guddn418@kimm.re.kr (H.-U.K.)  
† These authors contributed equally to this work.



**Citation:** Kang, M.; Jang, S.K.; Kim, J.; Kim, S.; Kim, C.; Lee, H.-C.; Kang, W.; Choi, M.S.; Kim, H.; Kim, H.-U. Multi-Domain Data Integration for Plasma Diagnostics in Semiconductor Manufacturing Using Tri-CycleGAN. *J. Sens. Actuator Netw.* **2024**, *13*, 75. <https://doi.org/10.3390/jsan13060075>

Academic Editors: Manolo Dulva Hina and Amar Ramdane-Cherif

Received: 2 October 2024

Revised: 28 October 2024

Accepted: 31 October 2024

Published: 4 November 2024



**Copyright:** © 2024 by the authors. Licensee MDPI, Basel, Switzerland. This article is an open access article distributed under the terms and conditions of the Creative Commons Attribution (CC BY) license (<https://creativecommons.org/licenses/by/4.0/>).

**Abstract:** The precise monitoring of chemical reactions in plasma-based processes is crucial for advanced semiconductor manufacturing. This study integrates three diagnostic techniques—Optical Emission Spectroscopy (OES), Quadrupole Mass Spectrometry (QMS), and Time-of-Flight Mass Spectrometry (ToF-MS)—into a reactive ion etcher (RIE) system to analyze CF<sub>4</sub>-based plasma. To synchronize and integrate data from these different domains, we developed a Tri-CycleGAN model that utilizes three interconnected CycleGANs for bi-directional data transformation between OES, QMS, and ToF-MS. This configuration enables accurate mapping of data across domains, effectively compensating for the blind spots of individual diagnostic techniques. The model incorporates self-attention mechanisms to address temporal misalignments and a direct loss function to preserve fine-grained features, further enhancing data accuracy. Experimental results show that the Tri-CycleGAN model achieves high consistency in reconstructing plasma measurement data under various conditions. The model's ability to fuse multi-domain diagnostic data offers a robust solution for plasma monitoring, potentially improving precision, yield, and process control in semiconductor manufacturing. This work lays a foundation for future applications of machine learning-based diagnostic integration in complex plasma environments.

**Keywords:** plasma diagnostics; reactive ion etching (RIE); semiconductor manufacturing; machine learning; cycle-consistent adversarial network (CycleGAN); multi-domain data integration

## 1. Introduction

Technological advancements in artificial intelligence (AI), the Internet of Things (IoT), and high-performance computing are driving modern innovation, all of which rely heavily on advanced semiconductor technologies [1]. For example, AI applications require specialized hardware to run complex machine learning algorithms efficiently, IoT devices must integrate various functionalities into compact designs, and high-performance computing systems depend on High-Bandwidth Memory (HBM) to handle large-scale data

processing and computation quickly and effectively. Meeting the stringent performance requirements of these applications necessitates the use of plasma-based processes, including deposition [2,3], etching [4–9], and cleaning [10,11]. These processes are essential for achieving the high precision and efficiency needed in advanced semiconductor device fabrication. Plasma generates reactive species that facilitate precise atomic-level material modifications, making it indispensable for high-aspect-ratio etching and other critical processes in semiconductor manufacturing. Accurate monitoring of the chemical reactions and behaviors of these reactive species is crucial for maintaining the precision and consistency of plasma-based manufacturing processes. Process analysis and control, driven by monitoring data, not only optimize production but also help reduce defects, ultimately improving yield and ensuring the efficient manufacturing of high-performance semiconductor devices.

The generation of plasma involves the formation of several key components, including radicals, ions, neutral species, and excited electrons, which subsequently emit light [12]. To effectively monitor and control the chemical reactions within plasma, it is essential to diagnose its state during the process using various methods [13]. Optical Emission Spectroscopy (OES) is one of the most widely used diagnostic techniques, as it is non-invasive and capable of real-time monitoring without disrupting the plasma environment [14–17].

OES analyzes the light emitted from excited radicals at various wavelengths, offering crucial insights into the electron energy levels of different species within the plasma [18]. However, it faces limitations, particularly in detecting species with low emission intensities or those that do not emit visible light, which can result in incomplete diagnostics. On the other hand, mass spectrometry-based techniques, such as Quadrupole Mass Spectrometry (QMS) [17,19,20] and Time-of-Flight Mass Spectrometry (ToF-MS) [21,22], provide a more comprehensive detection capability, including neutral species and those with low emission characteristics, offering a more complete picture of the plasma state. Nevertheless, both QMS and ToF-MS are invasive, requiring the extraction of gas samples from the chamber, which may disturb the plasma. Furthermore, unstable species critical to plasma processes can degrade during sampling, reducing the accuracy of the diagnostics.

To address these challenges, we employed machine learning to integrate data from the three diagnostic techniques, offering a method to complement their strengths and mitigate their respective limitations. Machine learning has shown its potential in various fields to handle complex, high-dimensional datasets, enabling more accurate and efficient analysis across different domains [23,24]. Machine learning techniques such as deep learning and neural networks have been successfully applied to process large volumes of data that are challenging to interpret with traditional methods. Among these, Cycle-Consistent Generative Adversarial Network (CycleGAN) is particularly useful for transforming data between different domains without requiring paired datasets [25]. While primarily applied to image domain transformations, we adapted this technique to integrate data from different semiconductor process diagnostic methods.

In our experimental setup, we connected the three diagnostic techniques (OES, QMS, and ToF-MS) to an inductively coupled plasma reactive ion etching (ICP-RIE) system, enabling systematic data collection under various plasma conditions. To analyze the diverse data from these diagnostic methods, we developed the Triangular Cycle-Consistent Generative Adversarial Network (Tri-CycleGAN). In contrast to conventional CycleGAN models, which are typically constrained to two domains, our approach demonstrates the capacity to transform data between three distinct domains, illustrating the potential for broader application to other semiconductor diagnostic techniques. To further enhance the accuracy of data transformation between domains, we introduced self-attention mechanisms and a custom loss function into the transformation model, improving feature extraction and optimizing the consistency of data integration across the three diagnostic techniques. By leveraging the strengths of all three diagnostic techniques, we were able to overcome the limitations of each individual method, resulting in a more comprehensive understanding of the plasma state. Additionally, cross-referencing overlapping spectral data from OES and mass data from QMS and ToF-MS enabled more precise identification of the species

generated in the plasma. This novel approach not only facilitates comprehensive plasma diagnostics but also presents a framework that can be extended to various other plasma-based processes and semiconductor equipment, including PECVD, sputtering, and PEALD.

## 2. Experimental Setup and Data Transformation

In this study, an ICP-RIE system (RAINBOW 4420, Lam Research, Fremont, CA, USA) was employed for plasma etching experiments, as shown on the left side of Figure 1a. A high-density plasma was generated by applying radio-frequency (RF) power at 13.56 MHz to the copper coil, while a separate RF generator controlled the DC bias voltage through the bottom electrode. Before the etching process, the chamber was evacuated to a base pressure of  $10^{-6}$  Torr using a turbomolecular pump (BOC Edwards, Burgess Hill, UK), ensuring a clean and stable environment. To remove any contaminants before data collection, a cleaning step was performed. A gas mixture of 50 sccm of Ar and 20 sccm of O<sub>2</sub> was introduced, while 250 W of RF power was applied to the top coil for 5 min. This procedure helped eliminate any residual particles or impurities, ensuring that subsequent measurements would be accurate and uncontaminated.

After the cleaning process, a SiO<sub>2</sub> wafer was placed in the chamber, and the etching process was carried out using a gas mixture of CF<sub>4</sub>, Ar, and O<sub>2</sub>. To achieve stable plasma across a wide range of process conditions using Penning ionization [26], we introduced Ar and O<sub>2</sub> gases at a flow rate of 10 sccm each. Based on typical gas composition ratios for CF<sub>4</sub>, Ar, and O<sub>2</sub> plasma etching, the CF<sub>4</sub> flow was varied across four conditions, 5, 10, 15, and 20 sccm, while maintaining the chamber pressure at 20 mTorr. The RF power applied to the top coil was adjusted from 50 W to 110 W in 10 W increments across seven conditions. This resulted in 28 combinations of gas flow and power levels. For each condition, data were collected across three diagnostic domains (OES, QMS, and ToF-MS), targeting 8 key process gases. Each collection was repeated three times to ensure sufficient data for model training and testing.

Data were collected using three diagnostic techniques during the etching process to monitor the plasma characteristics in real time. OES (Maya2000Pro, Ocean Insight, Orlando, FL, USA) was employed due to its non-invasive nature, ease of implementation, and fast measurement capabilities. OES captures real-time light emissions from excited species in plasma. In a plasma environment mixed with O<sub>2</sub>, CF<sub>4</sub> is prone to decompose into CF<sub>3</sub>, CF<sub>2</sub>, and CF due to the high energy conditions within the plasma. During the ionization process in QMS and ToF-MS diagnostics, CF<sub>4</sub> decomposes into CF<sub>3</sub>, CF<sub>2</sub>, and CF, making it difficult to detect [27]. Consequently, CF<sub>3</sub>, CF<sub>2</sub>, and CF were selected for analysis to ensure consistency in monitoring the chemical species present in the plasma. Key species expected to form during the etching process were selected, each corresponding to specific emission wavelengths: F-radical at 703 nm [28], CF<sub>3</sub> at 241.7 nm [29], CF<sub>2</sub> at 262.6 nm [30], CF at 255 nm [31], O<sub>2</sub> at 777 nm [32,33], CO<sub>2</sub> at 357 nm [34], CO at 519.82 nm [35], and COF at 258 nm [29].

During the etching process, in addition to collecting optical emissions, minimal amounts of gas were sampled and continuously monitored using QMS (PrismaPro QMG 250, Pfeiffer Vacuum, Aßlar, Germany) and ToF-MS (Itof, EL, Gwangmyeong, Republic of Korea), both of which were directly integrated with the main chamber. The QMS was able to detect species with mass ranges up to 200 and the ToF-MS system with mass ranges up to 500 amu. Key gas species detected during the process included F, CF<sub>3</sub>, CF<sub>2</sub>, CF, O<sub>2</sub>, CO<sub>2</sub>, CO, and COF, with molecular weights of 19, 69, 50, 31, 32, 44, 28, and 47 amu, respectively. However, there are inherent problems with gas sampling techniques, such as sampling delays and degraded temporal resolution due to the dead volume of the gas sampling interface. These limitations have been a critical challenge in synchronizing data across different diagnostic domains. Consequently, previous analyses were routinely fragmented, relying on isolated diagnostic techniques rather than an integrated approach.

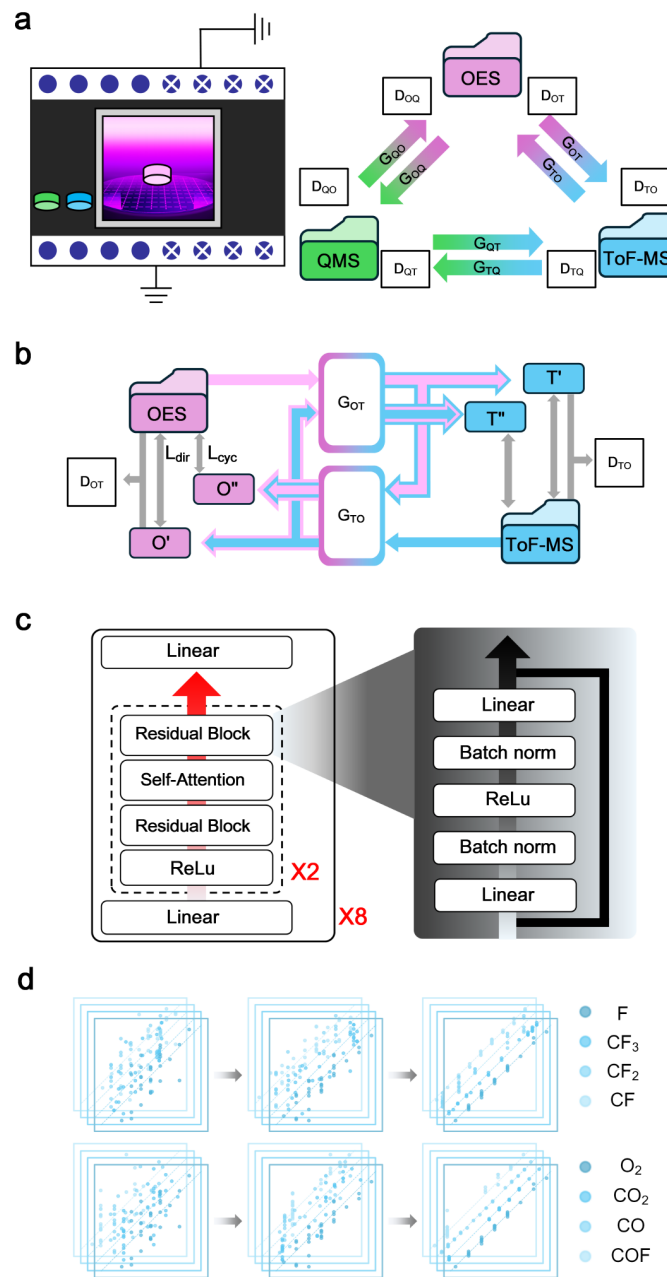


**Figure 1.** Experimental setup and Tri-CycleGAN architecture for multi-domain plasma diagnostics. (a) Schematic of the ICP-RIE system with integrated diagnostic techniques (OES, QMS, and ToF-MS). The arrows show data flow and transformations between diagnostic domains using the Tri-CycleGAN model (b) A segment of the Tri-CycleGAN model, illustrating data transformation between OES and ToF-MS domains using generators ( $G_{TO}$ ,  $G_{OT}$ ) and discriminators ( $D_{OT}$ ,  $D_{TO}$ ). (c) Generator network architecture with repeated blocks to learn transformations for each of the eight gas species using linear layers, residual blocks, and self-attention mechanisms. (d) Alignment between real and reconstructed data for eight gas species (F,  $CF_3$ ,  $CF_2$ , CF,  $O_2$ ,  $CO_2$ , CO, and COF), demonstrating improved matching of distributions as training advances.

To address these challenges and achieve seamless integration of data across different diagnostic domains, we employed a Cycle-Consistent Generative Adversarial Network (CycleGAN) model tailored for multi-domain transformation. CycleGAN is a deep learning model widely used for translating data between two distinct domains without requiring paired training data [36–39]. It consists of two generators and two discriminators, where each generator learns to map data from one domain to another, and each discriminator

evaluates the authenticity of the generated data. To ensure consistency during domain translation, CycleGAN introduces a cycle consistency loss that preserves the content by enabling the generated data to be mapped back to their original form in the source domain.

In our study, we applied this CycleGAN framework to synchronize data collected using three diagnostic techniques. Specifically, we utilized three separate CycleGAN models to enable data transformation between each pair of diagnostic techniques, effectively covering all possible domain combinations. As shown on the right side of Figure 1a, the Tri-CycleGAN consists of six generators and six discriminators that facilitate data transformation between OES, QMS, and ToF-MS. OES, QMS, and ToF-MS data are represented in pink, green, and blue, respectively, to distinguish the data obtained from each diagnostic technique. The model includes generators ( $G_{QO}$ ,  $G_{OQ}$ ,  $G_{OT}$ ,  $G_{TO}$ ,  $G_{QT}$ , and  $G_{TQ}$ ), and discriminators ( $D_{QO}$ ,  $D_{OQ}$ ,  $D_{OT}$ ,  $D_{TO}$ ,  $D_{QT}$ , and  $D_{TQ}$ ). The generators transform data from one domain into another [36]. For instance,  $G_{QO}$  generates fake OES data from QMS data. The generator is represented by arrows with gradual color changes, symbolizing the transformation of data between different domains. The discriminators, on the other hand, are responsible for evaluating the authenticity of the generated data. For instance,  $D_{OQ}$  determines whether the OES data generated by  $G_{QO}$  are real or fake. The generators and discriminators work in tandem, where the generator attempts to transform data between domains, and the discriminator evaluates the authenticity of the transformed data.

Figure 1b shows the Tri-CycleGAN model between the OES and ToF-MS data domains in detail. Generators ( $G_{OT}$  and  $G_{TO}$ ) are responsible for transforming data between OES and ToF-MS. In the OES and ToF-MS data domains, the transformation process is defined as follows:

$$O' = G_{TO}(T), \quad T' = G_{OT}(O) \tag{1}$$

where  $O'$  and  $T'$  represent the generated fake data in the ToF-MS and OES domains, respectively. In the model schematic of Figure 1b, the arrows indicate the flow of data, where the internal color represents the original domain and the border color represents the transformed domain. The data are then reconstructed back into their original domain as follows:

$$O'' = G_{TO}(O'), \quad T'' = G_{OT}(T') \tag{2}$$

To effectively learn transformations between the two domains, the model is trained using a combination of three loss functions: the adversarial loss ( $L_{GAN}$ ), which aligns the generated data with real data distributions; the cycle consistency loss ( $L_{cyc}$ ), which maintains the original structure of data after round-trip transformations; and the direct loss ( $L_{dir}$ ), which we introduced to improve transformations between time-dependent 1D measurement data obtained from real plasma etching processes using different diagnostic techniques. While  $L_{GAN}$  and  $L_{cyc}$  are conventional loss functions widely used in CycleGAN models,  $L_{dir}$  specifically ensures accurate alignment and feature preservation across these distinct data sources [40–42].

The first component, the adversarial loss ( $L_{GAN}$ ) is applied to both the OES and ToF-MS data domains to ensure that the generated data ( $O'$ ,  $T'$ ) are indistinguishable from real data in the respective target domains. This objective is achieved by minimizing the following expression:

$$L_{GAN} = \mathbb{E}_{T \sim p_{data}(T)} \left[ (D_{OT}(G_{TO}(T)) - 1)^2 \right] + \mathbb{E}_{O \sim p_{data}(O)} \left[ (D_{TO}(G_{OT}(O)) - 1)^2 \right] \tag{3}$$

The first term makes the ToF-MS data transformed to the OES domain ( $O'$ ) resemble the real OES data, and the second term makes the OES data transformed to the ToF-MS domain ( $T'$ ) match the real ToF-MS data. However, minimizing adversarial loss alone may lead to loss of unique features during domain transformation [43]. Therefore, the cycle

consistency loss  $L_{cyc}$  is introduced to preserve the original structure of the data during domain transformations. It is defined as

$$L_{cyc} = \mathbb{E}_{T \sim p_{data}(T)} [\|G_{OT}(G_{TO}(T)) - T\|_1] + \mathbb{E}_{O \sim p_{data}(O)} [\|G_{TO}(G_{OT}(O)) - O\|_1] \quad (4)$$

The first term computes the  $L_1$ -norm between the ToF-MS data, transformed to the OES domain and then back to the ToF-MS domain ( $T$  and  $T''$ ), and the real ToF-MS data. Similarly, the second term computes the  $L_1$ -norm between ( $O$  and  $O''$ ).

In the conventional CycleGAN framework, generally using expectation-based loss prioritizes aligning the overall data distribution between domains [37–39], but it often fails to capture detailed individual characteristics. This limitation is particularly problematic in reliability-critical systems like plasma monitoring in semiconductor manufacturing, where capturing not only the unique features of each diagnostic techniques but also the anomaly signals and faults occurring during the process is crucial. Anomalies and fault signals are often rare and localized, making them difficult to detect when only considering average distributional differences between domains.

To address this issue, our research incorporates a direct loss function alongside the expectation-based loss. The direct loss is defined as

$$L_{dir} = \|O - G_{TO}(T)\|_1 + \|T - G_{OT}(O)\|_1 \quad (5)$$

The complete generator loss function is then formulated as

$$L_G = L_{GAN} + \lambda_{cycle} \times L_{cyc} + \lambda_{direct} \times L_{dir} \quad (6)$$

where  $L_{GAN}$  represents the adversarial loss,  $L_{cyc}$  is the cycle consistency loss, and  $L_{dir}$  is the direct loss defined above. The weights  $\lambda_{cycle}$  and  $\lambda_{direct}$  control the relative importance of the cycle consistency and direct losses, respectively. The weights were selected based on existing literature [25,44] and empirical testing to balance transformation accuracy and stability.  $\lambda_{direct}$  was adjusted to balance against the cycle consistency and adversarial losses.

By utilizing paired data collected during experiments [45], the direct loss function addresses issues such as overfitting and mode collapse. These issues are particularly critical for 1D semiconductor data transformation, where preserving physical characteristics precisely is essential. Directly comparing the transformed data with real data enables the model to capture subtle discrepancies and transient fault signals that might not be evident in the overall data distribution.

Models without the direct loss function can capture distinct features such as plasma on/off states, but may struggle with offsets and scale differences in the generated data. This is due to mode collapse, where different plasma conditions produce similar outputs because of the high similarity between input data [46,47]. The direct loss function penalizes the model more heavily when mode collapse occurs, as it produces high errors in these cases. This ensures that the model is pushed to generate more diverse and accurate outputs by avoiding repetitive patterns or misrepresentations in the data, especially when dealing with highly similar input conditions.

Figure 1c illustrates the architecture of the generator model, designed to process time-dependent 1D measurement data [48] obtained from real plasma etching processes using various diagnostic techniques. Experimental data were collected by varying the RF power between 50 and 110 W and the  $CF_4$  flow rate between 5 and 20 sccm. These data were then used to train the model, enabling it to accurately capture the plasma behavior under different operating conditions. The generator has two sets of residual blocks [49] stacked twice, making a total of eight residual layers. Each block extracts features and learns nonlinear transformations, while the residual connections help prevent gradient vanishing, ensuring stable training for deep networks.

To address the timing discrepancies between different diagnostic techniques, such as OES, QMS, and ToF-MS, a self-attention mechanism [50] is incorporated into the model.

When data are collected through different mechanisms and equipment, slight temporal offsets can occur, leading to misalignments. The self-attention mechanism helps reduce these temporal misalignments by evaluating the importance of each data point in relation to others across the entire sequence [51]. This enables the generator to transform and represent data from multiple diagnostic techniques, ensuring accurate modeling of plasma dynamics. Additionally, the model is structured to handle the eight key chemical species in  $\text{CF}_4$  plasma by building separate pathways, which allows for specialized learning and robust performance in multi-domain data transformations.

Figure 1d visualizes the alignment between the reconstructed data  $T''$  and the real data  $T$  in the ToF-MS domain for eight chemical species: F,  $\text{CF}_3$ ,  $\text{CF}_2$ , CF,  $\text{O}_2$ ,  $\text{CO}_2$ , CO, and COF. Each plot represents the degree of similarity between the distributions of the real and reconstructed data. As training progressed, the model minimized reconstruction errors, ensuring that the data closely matched between the real and reconstructed states.

Unlike traditional models such as Kalman filters, which process data sequentially [52], Tri-CycleGAN offers a computational advantage by transforming the entire dataset in parallel once the model has been trained. This parallel processing reduces computational time, allowing for faster data transformations across multiple domains like OES, QMS, and ToF-MS. Additionally, since the model learns complex nonlinear relationships, it maintains minimal reconstruction error when processing normal data. However, since the model is trained to accurately transform only normal data, the reconstruction error increases significantly after abnormal data undergoes both the transformation and reverse transformation process [53]. This contrast between low reconstruction error for normal data and high error for abnormal data allows for efficient differentiation between the two. These advantages in both speed and anomaly detection make Tri-CycleGAN highly suitable for process monitoring and diagnostics in semiconductor environments.

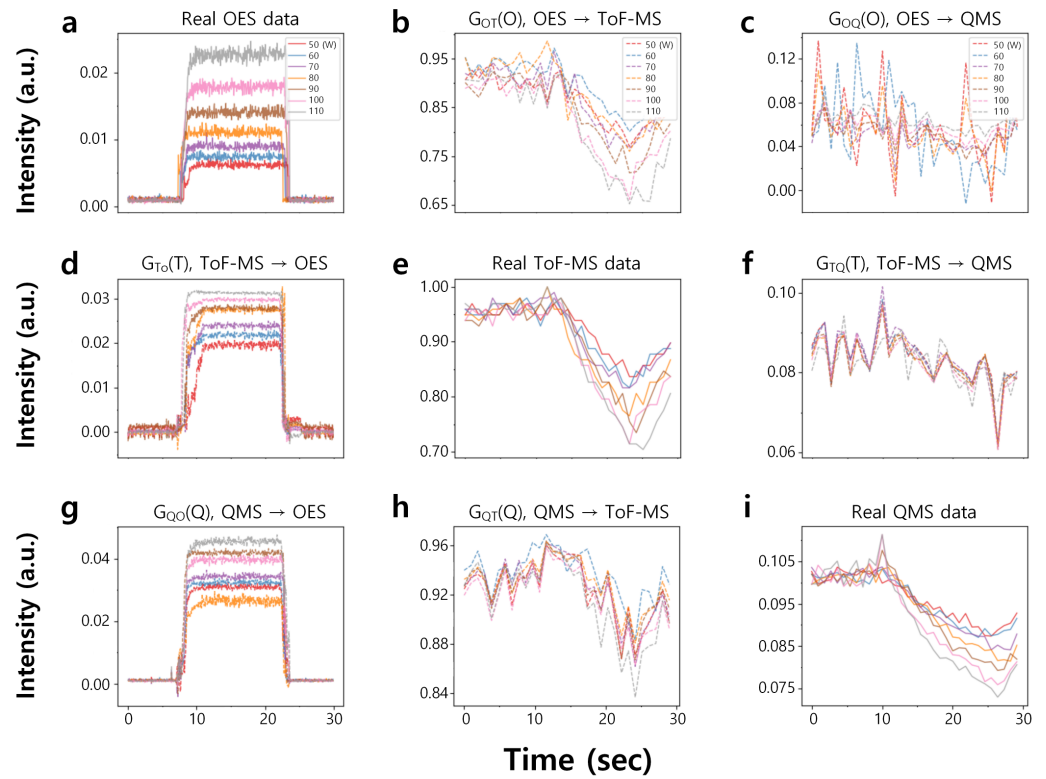
### 3. Results and Discussion

Figure 2 illustrates the multi-domain transformations of  $\text{CF}_3$  data across OES, ToF-MS, and QMS domains. The test data were input as  $\text{CF}_3$ , collected under RF power levels ranging from 50 to 110 W with a  $\text{CF}_4$  flow rate of 20 sccm.  $\text{CF}_3$  was selected as the test species because it serves as the primary source of highly reactive F-radicals. These radicals play a critical role in the plasma etching process. This demonstrates that the model has been sufficiently trained to perform accurate transformations across domains and effectively capture the variations in  $\text{CF}_3$  under different experimental conditions.

Figure 2 is organized into three rows and three columns, each representing different combinations of real and generated data in the respective domains. The first row (Figure 2a–c) shows the real OES data (Figure 2a) and the generated data in the ToF-MS (Figure 2b) and QMS (Figure 2c) domains translated from the OES domain. The second row (Figure 2d–f) represents transformations starting from the ToF-MS domain, where Figure 2e displays the real ToF-MS data, and Figure 2d,f show the data translated into the OES and QMS domains, respectively. Similarly, the third row (Figure 2g–i) illustrates transformations from the QMS domain, with the real QMS data in Figure 2i and their translations into the OES (Figure 2g) and ToF-MS (Figure 2h) domains.

Each column represents a different target domain for transformation. The first column (Figure 2a,d,g) shows OES data, including the real OES data and the OES data generated from the other domains. The second column (Figure 2b,e,h) displays data translated into the ToF-MS domain, while the third column (Figure 2c,f,i) presents data in the QMS domain. In all plots, the real data are represented by solid lines, while the generated data are depicted by dashed lines. Other process gases, such as  $\text{O}_2$  and the F-radical, are also included in the Supporting Materials (Figures S1 and S2). Due to its high reactivity, the F-radical was scarcely detected in the ToF-MS and QMS diagnostic techniques, as it tends to adsorb onto surfaces in the gas line during transport to the measurement devices. However, clear plasma emissions for F-radicals were observed in the OES data. Our model successfully captured these signals at the corresponding locations in the generated data, as shown in

the outputs of  $G_{TO}(T)$  and  $G_{QO}(Q)$ . This confirms that our approach can bridge the gap between domains with disparate diagnostic techniques and maintain high consistency even under challenging conditions.



**Figure 2.** Multi-domain transformations of  $CF_3$  data across OES, ToF-MS, and QMS diagnostic techniques using the Tri-CycleGAN model. Each row corresponds to a different original domain: OES (a–c), ToF-MS (d–f), and QMS (g–i). Each column represents the target domain for transformation: OES, ToF-MS, and QMS, respectively. Diagonal subplots (a,e,i) show the real data from each domains, while off-diagonal subplots illustrate transformed data in the target domains. Solid lines indicate real data, and dashed lines represent transformed data.

The Tri-CycleGAN model demonstrated robustness in integrating diverse diagnostic techniques through multi-domain transformations, proposing a novel approach to integrate previously fragmented semiconductor process diagnostic data. Although discrepancies may arise between generated and real data due to factors such as measurement noise, temporal resolution mismatches among diagnostic methods, and gas transmission delays caused by equipment interfaces, these issues can be mitigated through additional measurements, equipment parameter control, and implementing calibration procedures such as domain adaptation and transfer learning [48] to minimize the discrepancies.

Figure 3 illustrates the training progress of the Tri-CycleGAN model for  $CF_3$  data transformations between OES, QMS, and ToF-MS domains. Test data, collected under a  $CF_4$  flow rate of 10 sccm and an RF power of 50 W, were input into models trained for 0, 500, and 1000 epochs, as well as the fully trained model. In each graph, the black line indicates the real data, the red line represents the generated data in the target domain, and the blue line shows the reconstructed data after being transformed back to the source domain. The figure is divided into three main sections: (a–h) show transformations between OES and QMS domains, (i–p) show transformations between QMS and ToF-MS domains, and (q–x) show transformations between OES and ToF-MS domains.



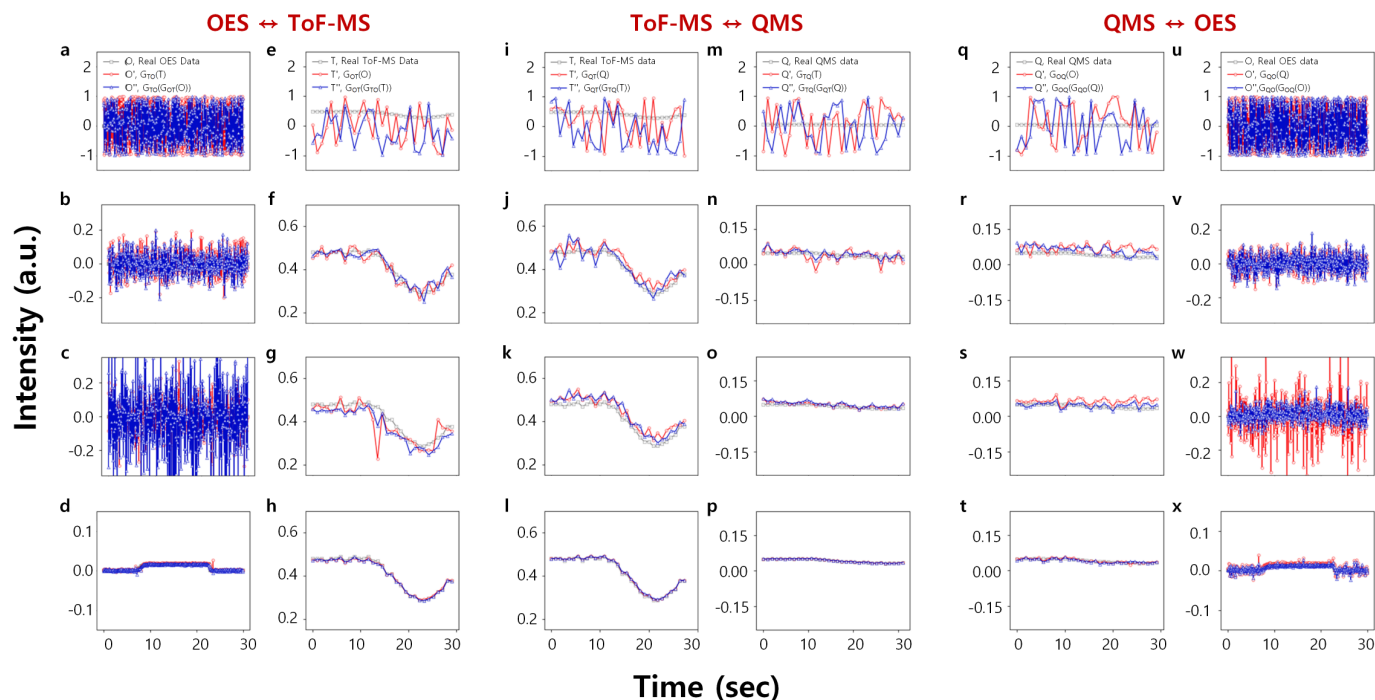


**Figure 3.** Training progress of the Tri-CycleGAN model for  $\text{CF}_3$  data transformations across the OES, QMS, and ToF-MS domains. Sections (a–h), (i–p), and (q–x) show transformations between OES and QMS, QMS and ToF-MS, and OES and ToF-MS domains, respectively. Columns represent different training stages: initial state (epoch 0), epoch 500, epoch 1000, and the fully trained model. In each plot, black lines show the real data, red lines indicate generated data, and blue lines represent reconstructed data.

Each section is further organized into four columns, representing different training epochs: epoch 0 (first column), epoch 500 (second column), epoch 1000 (third column), and the fully trained model (fourth column). In the initial state (epoch 0), the generated data are completely random as the model has not yet learned any domain mappings. As training progresses to epoch 500 and epoch 1000, competition between the generator and discriminator causes fluctuations in the generated data. However, the model gradually reduces errors and converges to the real data, effectively capturing their temporal patterns in the fully trained stage.

The results clearly demonstrate effective learning, even under conditions with low gas flow rates and low plasma power, which often produce weak signal intensities. Despite these challenging scenarios,  $\text{CF}_3$  signals are successfully reconstructed across domains, showing robust convergence and high consistency in data translation between distinct diagnostic techniques. The training progress for the input gas  $\text{O}_2$  and the F-radical is provided in the Supporting Materials (Figures S3 and S4).

Figure 4 compares the generated and reconstructed data for  $\text{CF}_3$ , F-radical, and  $\text{O}_2$  across OES, ToF-MS and QMS domains based on test data collected under a  $\text{CF}_4$  flow rate of 10 sccm and an RF power of 50 W. The first row (Figure 4a–c) shows  $\text{CF}_3$  data transformations in the OES, ToF-MS and QMS domains, comparing the generated and reconstructed data with the real data. The second row (Figure 4d–f) and the third row (Figure 4g–i) show the transformations of F-radical and  $\text{O}_2$  data in the OES, ToF-MS and QMS domains, respectively. In addition to these species, we also collected data for five other gas species ( $\text{CF}_2$ , CF, COF,  $\text{CO}_2$ , and CO) during the experiments, and the comparison results for these five models across the three diagnostic domains are provided in the Supporting Materials (Figure S5). This comprehensive analysis demonstrates the model's effectiveness in capturing and translating data for various chemical species across different diagnostic techniques.

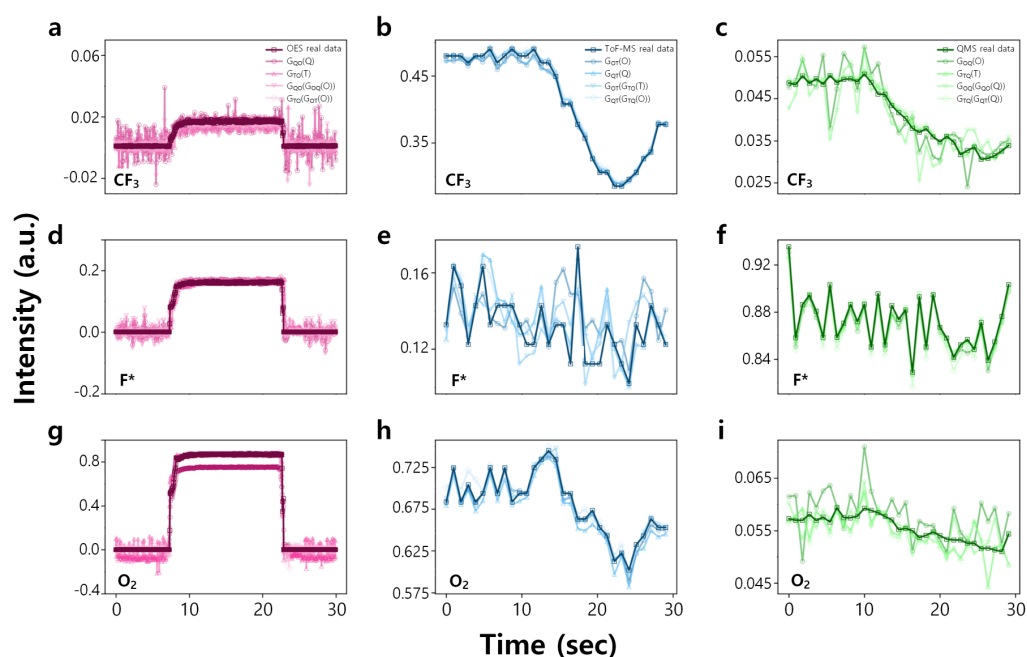


**Figure 4.** Comparison of real data, generated data from different source domains and the reconstructed data from different transformation pathways for  $\text{CF}_3$ , F-radical, and  $\text{O}_2$  across OES, ToF-MS, and QMS domains. The first row (a–c) shows  $\text{CF}_3$  transformations in each domain, while the second (d–f) and third rows (g–i) display transformations for the F-radical and  $\text{O}_2$ , respectively.

The Tri-CycleGAN model performs consistent transformations across the OES, ToF-MS, and QMS domains for three species:  $\text{CF}_3$ , F-radical, and  $\text{O}_2$ . The transformed data generally align well with the real data, showing that the model captures the key features of the input data despite variations in amplitude and noise across domains. These results indicate that the model can effectively integrate multi-domain data, making it suitable for multi-domain analysis of complex semiconductor plasma processes.

Figure 5 illustrates the changes in the loss functions during the training process of the Tri-CycleGAN model on a logarithmic scale. It provides individual loss values for  $\text{CF}_3$  (Figure 5a–c) as well as the mean loss values for all species (Figure 5d–f), including F,  $\text{CF}_3$ ,  $\text{CF}_2$ , CF,  $\text{O}_2$ ,  $\text{CO}_2$ , CO, and COF. The black line indicates the generator loss, and the red and blue lines represent the discriminator losses for different domains. The detailed loss function trends for the remaining species are provided in the Supporting Materials (Figure S6).

For  $\text{CF}_3$  (Figure 5a–c), the generator loss (black line) starts at a high value and rapidly decreases as the training progresses, indicating that the generator quickly learns to produce data similar to the real data. As the generator's performance improves, the discriminator loss increases, suggesting that it struggles to differentiate between real and generated samples. Eventually, both the generator and discriminator losses converge and stabilize, indicating that the two networks have reached an equilibrium, which is a typical sign of successful Tri-CycleGAN training [25].

More specifically, for the OES to ToF-MS transformation model (Figure 5a), the loss values show stabilization around 5k epochs. This period reflects when the model has learned to handle the transformation between these two domains effectively. After 16k epochs, a further decrease in loss indicates additional fine-tuning in the generator's performance. The other two transformation models, ToF-MS to QMS (Figure 5b) and QMS to OES (Figure 5c), show more regular patterns after approximately 4k epochs, highlighting the more consistent performance in these transformations. This stability suggests that the generator has successfully learned the relationships between the data from these domains earlier in the training process.

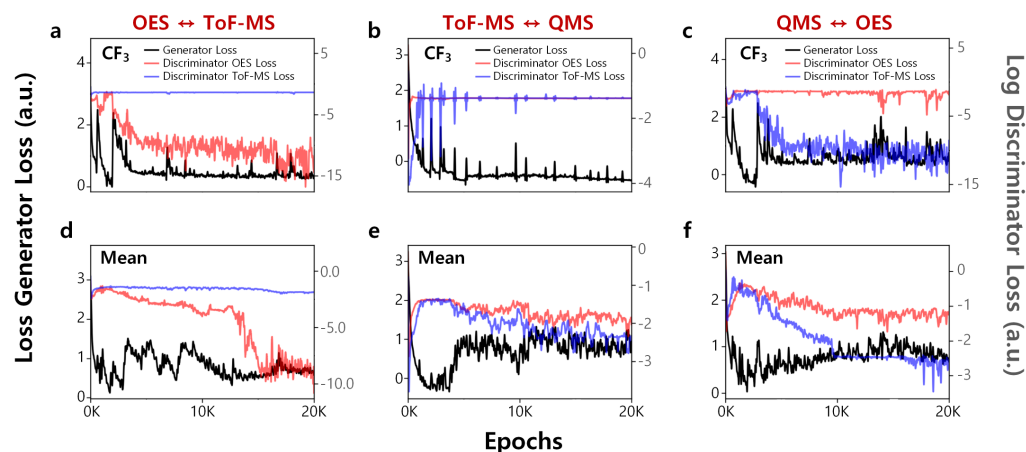


**Figure 5.** Logarithmic changes in the loss functions during the training process of the Tri-CycleGAN model. The left  $y$ -axis shows the generator loss, while the right  $y$ -axis displays the discriminator loss. (a–c) present loss values for  $CF_3$ , and (d–f) show the mean loss values for all species ( $CF_2$ , CF, F-radical, COF,  $CO_2$ , CO, and  $O_2$ ). Black lines indicate generator loss, while red and blue lines represent discriminator losses for different domains (OES, QMS, and ToF-MS).

The mean loss values for all species (Figure 5d–f) follow a similar pattern to the individual  $CF_3$  loss values. The mean generator loss decreases rapidly at the beginning and stabilizes at a low value, showing that the generator achieves a stable performance across multiple species. The mean discriminator loss values exhibit steady fluctuations but overall maintain a relatively constant level after an initial phase of rapid changes. This suggests that the multi-domain transformations are consistent across different diagnostic techniques and that the model successfully captures the relationships between the different domains for all species. The stable loss values across domains confirm that the Tri-CycleGAN model is effective in transforming data between different measurement domains, indicating its robustness in integrating multi-domain plasma diagnostics.

#### 4. Conclusions

We have developed a methodology to integrate multiple diagnostic techniques for monitoring and analyzing plasma conditions, which are essential for semiconductor manufacturing processes. To address the limitations of conventional diagnostic technique, we combined OES, QMS and ToF-MS to identify and monitor key chemical species within  $CF_4$ -based plasma. By leveraging the unique strengths of each diagnostic technique, our integrated approach provides a more comprehensive understanding of the plasma state, thereby improving the precision and efficiency of semiconductor fabrication.

This research proposes a Tri-CycleGAN model specifically designed for multi-domain data transformations in semiconductor process diagnostics. The model integrates multi-domain plasma diagnostics (OES, QMS, and ToF-MS), enabling effective data mapping across these different diagnostic techniques. By incorporating self-attention mechanisms to correct for temporal misalignments and a direct loss function to preserve fine-grained details, the model ensures more accurate and reliable data transformations. These improvements allow it to capture subtle but critical plasma variations, enhancing the precision of diagnostics. As the model is trained to synthesize data across multiple measurement domains, it effectively eliminates the need for redundant diagnostic techniques, offering a cost-efficient solution for complex diagnostic environments. This not only reduces operational costs but also leads to more reliable process monitoring and better decision-making in semiconductor manufacturing.

This approach not only minimizes the reliance on multiple diagnostic techniques but also offers a solution for deriving a comprehensive understanding of the plasma state using limited data sources. The proposed framework can also serve as a basis for building

more advanced diagnostic models that adapt to various plasma-based manufacturing environments, potentially improving process control, yield, and overall efficiency in semiconductor production.

**Supplementary Materials:** The following supporting information can be downloaded at <https://www.mdpi.com/article/10.3390/jsan13060075/s1>, Figures S1 and S2: Multi-domain transformations of F-radical and O<sub>2</sub> data, Figures S3 and S4: Training progress of the Tri-CycleGAN model for F-radical and O<sub>2</sub> data, Figure S5: Comparison of real data, generated data, and the reconstructed data, Figure S6: Logarithmic changes in the loss functions.

**Author Contributions:** Conceptualization, M.K. and S.K.J.; methodology, M.K., S.K.J. and J.K.; software, S.K.J. and J.K.; validation, C.K., H.-C.L., W.K. and H.-U.K.; formal analysis, M.K. and S.K.J.; investigation, M.K. and S.K.J.; resources, H.-C.L., W.K., M.S.C., H.K. and H.-U.K.; data curation, M.K. and H.-U.K.; writing—original draft preparation, M.K. and S.K.; writing—review and editing, M.S.C., H.K. and H.-U.K.; visualization, S.K.J. and J.K.; supervision, H.K. and H.-U.K.; project administration, H.-U.K.; funding acquisition, H.K. and H.-U.K. All authors have read and agreed to the published version of the manuscript.

**Funding:** This work was supported by K-CHIPS (Korea Collaborative & High-tech Initiative for Prospective Semiconductor Research) (KEIT1415187508, 20024772) funded by the Ministry of Trade, Industry & Energy (MOTIE, Korea) and KIMM institutional program (NK248E, NK251E) and NST/KIMM. This work was also supported by the Material Innovation Leading Project through the National Research Foundation of Korea (NRF) funded by the Ministry of Science and ICT (2020M3H4A3081879).

**Data Availability Statement:** The data that support the findings of this study are available from the corresponding author upon reasonable request.

**Conflicts of Interest:** The authors declare no conflicts of interest.

## References

1. Ross, P.; Maynard, K. Towards a 4th industrial revolution. *Intell. Build. Int.* **2021**, *13*, 159–161. [[CrossRef](#)]
2. Konuma, M. *Film Deposition by Plasma Techniques*; Springer: Berlin/Heidelberg, Germany, 1992. [[CrossRef](#)]
3. Batey, J.; Tierney, E. Low-temperature deposition of high-quality silicon dioxide by plasma-enhanced chemical vapor deposition. *J. Appl. Phys.* **1986**, *60*, 3136–3145. [[CrossRef](#)]
4. Donnelly, V.M.; Kornblit, A. Plasma etching: Yesterday, today, and tomorrow. *J. Vac. Sci. Technol. A* **2013**, *31*, 050825. [[CrossRef](#)]
5. Coburn, J.W.; Winters, H.F. Plasma etching—A discussion of mechanisms. *J. Vac. Sci. Technol.* **1979**, *16*, 391–403. [[CrossRef](#)]
6. Kanarik, K.J.; Lill, T.; Hudson, E.A.; Sriraman, S.; Tan, S.; Marks, J.; Vahedi, V.; Gottscho, R.A. Overview of atomic layer etching in the semiconductor industry. *J. Vac. Sci. Technol. A* **2015**, *33*, 020802. [[CrossRef](#)]
7. Kim, C.; Kim, M.; Cho, D.; Kanade, C.; Seok, H.; Bak, M.; Kim, D.; Kang, W.; Kim, T.; Kim, H.U. First-Principles Calculation Guided High-Purity Layer Control of 4 in. MoS<sub>2</sub> by Plasma RIE. *Chem. Mater.* **2023**, *35*, 1016–1028. [[CrossRef](#)]
8. Kim, C.; Lee, S.; Kim, M.; Choi, M.S.; Kim, T.; Kim, H.U. Machine Learning-Based Prediction of Atomic Layer Control for MoS<sub>2</sub> via Reactive Ion Etcher. *Appl. Sci. Conver. Technol.* **2023**, *32*, 106–109. [[CrossRef](#)]
9. Kim, C.; Kim, M.; Kim, S.; Kang, M.; Choi, M.S.; Kim, H.U. Plasma and Gas-based Semiconductor Technologies for 2D Materials with Computational Simulation & Electronic Applications. *Adv. Electron. Mater.* **2024**, *10*, 2300835. [[CrossRef](#)]
10. Petasch, W.; Kegel, B.; Schmid, H.; Lendenmann, K.; Keller, H. Low-pressure plasma cleaning: A process for precision cleaning applications. *Surf. Coat. Technol.* **1997**, *97*, 176–181. [[CrossRef](#)]
11. Reinhardt, K.A.; Reidy, R.F. *Handbook for Cleaning for Semiconductor Manufacturing: Fundamentals and Applications*; John Wiley & Sons: Hoboken, NJ, USA, 2011.
12. Lieberman, M.A.; Lichtenberg, A.J. *Principles of Plasma Discharges and Materials Processing*; John Wiley & Sons: Hoboken, NJ, USA, 2005.
13. Gottscho, R.A.; Jurgensen, C.W.; Vitkavage, D.J. Microscopic uniformity in plasma etching. *J. Vac. Sci. Technol. B* **1992**, *10*, 2133–2147. [[CrossRef](#)]
14. Hershkowitz, N.; Breun, R.A. Diagnostics for Plasma Processing (Etching Plasmas) (Invited). *Rev. Sci. Instrum.* **1997**, *68*, 880–885. [[CrossRef](#)]
15. Akatsuka, H. Optical Emission Spectroscopic (OES) Analysis for Diagnostics of Electron Density and Temperature in Non-Equilibrium Argon Plasma Based on Collisional-Radiative Model. *Adv. Phys. X* **2019**, *4*, 1592707. [[CrossRef](#)]
16. Wang, S.; Wendt, A.; Boffard, J.; Lin, C.; Radovanov, S.; Persing, H. Noninvasive, real-time measurements of plasma parameters via optical emission spectroscopy. *J. Vac. Sci. Technol. A Vacuum Surfaces Film.* **2013**, *31*, 021303. [[CrossRef](#)]

17. Matsutani, A.; Ohtsuki, H.; Koyama, F.; Iga, K. Plasma Diagnostics in Inductively Coupled Plasma Etching Using Cl<sub>2</sub>/Xe. *Jpn. J. Appl. Phys.* **2000**, *39*, 1435. [[CrossRef](#)]
18. Boss, C.B.; Fredeen, K.J. *Concepts, Instrumentation, and Techniques in Inductively Coupled Plasma Optical Emission Spectrometry*, 2nd ed.; Perkin Elmer: Shelton, CT, USA, 1997.
19. An, S.R.; Choi, J.E.; Hong, S.J. In-situ process monitoring for eco-friendly chemical vapor deposition chamber cleaning. *J. Korean Phys. Soc.* **2021**, *79*, 1027–1036. [[CrossRef](#)]
20. Zimmermann, S.; Ahner, N.; Blaschta, F.; Schaller, M.; Rülke, H.; Schulz, S.E.; Gessner, T. Analysis of the impact of different additives during etch processes of dense and porous low-*k* with OES and QMS. *Microelectron. Eng.* **2010**, *87*, 337–342. [[CrossRef](#)]
21. Boesl, U. Time-of-flight mass spectrometry: Introduction to the basics. *Mass Spectrom. Rev.* **2017**, *36*, 86–109. [[CrossRef](#)]
22. Sasaki, K.S.K.; Ura, K.U.K.; Suzuki, K.S.K.; Kadota, K.K.K. Time-of-Flight Mass Spectrometry of Positive Ions in Helicon-Wave Excited High-Density CF<sub>4</sub> and C<sub>4</sub>F<sub>8</sub> Plasmas. *Jpn. J. Appl. Phys.* **1997**, *36*, 1282. [[CrossRef](#)]
23. Avital, N.; Nahum, E.; Levi, G.C.; Malka, D. Cognitive State Classification Using Convolutional Neural Networks on Gamma-Band EEG Signals. *Appl. Sci.* **2024**, *14*, 8380. [[CrossRef](#)]
24. Shabairou, N.; Cohen, E.; Wagner, O.; Malka, D.; Zalevsky, Z. Color Image Identification and Reconstruction Using Artificial Neural Networks on Multimode Fiber Images: Towards an All-Optical Design. *Opt. Lett.* **2018**, *43*, 5603–5606. [[CrossRef](#)]
25. Zhu, J.Y.; Park, T.; Isola, P.; Efros, A.A. Unpaired Image-to-Image Translation Using Cycle-Consistent Adversarial Networks. *arXiv* **2017**, arXiv:1703.10593. [[CrossRef](#)]
26. Nasser, E. *Fundamentals of Gaseous Ionization and Plasma Electronics*; Wiley-Interscience: New York, NY, USA, 1971.
27. Setareh, M.; Farnia, M.; Maghari, A.; Bogaerts, A. CF<sub>4</sub> Decomposition in a Low-Pressure ICP: Influence of Applied Power and O<sub>2</sub> Content. *J. Phys. D Appl. Phys.* **2014**, *47*, 355205. [[CrossRef](#)]
28. Gaboriau, F.; Cartry, G.; Peignon, M.C.; Cardinaud, C. Etching mechanisms of Si and SiO<sub>2</sub> in fluorocarbon ICP plasmas: Analysis of the plasma by mass spectrometry, Langmuir probe and optical emission spectroscopy. *J. Phys. D Appl. Phys.* **2006**, *39*, 1830. [[CrossRef](#)]
29. Suto, M.; Washida, N. Emission Spectra of CF<sub>3</sub> Radicals. II. Analysis of the UV Emission Spectrum of CF<sub>3</sub> Radicals. *J. Chem. Phys.* **1983**, *78*, 1012–1018. [[CrossRef](#)]
30. Kim, B.S.; Hong, S.J. Actinometric Investigation of In-Situ Optical Emission Spectroscopy Data in SiO<sub>2</sub> Plasma Etch. *Trans. Electr. Electron. Mater.* **2012**, *13*, 139–143. [[CrossRef](#)]
31. Guo, W.; Anantharajan, S.K.; Zhang, X.; Deng, H. A Study on the Damage Layer Removal of Single-Crystal Silicon Wafer after Atmospheric-Pressure Plasma Etching. *J. Micro -Nano-Manuf.* **2020**, *8*, 024501. [[CrossRef](#)]
32. Fragstein, F.V.; Schmachtenberg, E.; Hegenbart, A. Monitoring of Plasma Processes by OES. *Vak. Forsch. Prax.* **2007**, *19*, 39–43. [[CrossRef](#)]
33. Kregar, Z.; Bišćan, M.; Milošević, S.; Vesel, A. Monitoring Oxygen Plasma Treatment of Polypropylene with Optical Emission Spectroscopy. *IEEE Trans. Plasma Sci.* **2011**, *39*, 1239–1246. [[CrossRef](#)]
34. Khan, M.I.; Rehman, N.U.; Khan, S.; Ullah, N.; Masood, A.; Ullah, A. Spectroscopic study of CO<sub>2</sub> and CO<sub>2</sub>-N<sub>2</sub> mixture plasma using dielectric barrier discharge. *AIP Adv.* **2019**, *9*, 085015. [[CrossRef](#)]
35. Vassallo, E.; Cremona, A.; Ghezzi, F.; Ricci, D. Characterization by optical emission spectroscopy of an oxygen plasma used for improving PET wettability. *Vacuum* **2010**, *84*, 902–906. [[CrossRef](#)]
36. Goodfellow, I.J.; Pouget-Abadie, J.; Mirza, M.; Xu, B.; Warde-Farley, D.; Ozair, S.; Courville, A.; Bengio, Y. Generative Adversarial Networks. *arXiv* **2014**, arXiv:1406.2661. [[CrossRef](#)]
37. Nair, V.; Hinton, G.E. Rectified Linear Units Improve Restricted Boltzmann Machines. In Proceedings of the 27th International Conference on International Conference on Machine Learning (ICML'10), Haifa, Israel, 21–24 June 2010; pp. 807–814.
38. Ioffe, S.; Szegedy, C. Batch Normalization: Accelerating Deep Network Training by Reducing Internal Covariate Shift. *arXiv* **2015**, arXiv:1502.03167. [[CrossRef](#)]
39. LeCun, Y.; Boser, B.; Denker, J.S.; Henderson, D.; Howard, R.E.; Hubbard, W.; Jackel, L.D. Backpropagation Applied to Handwritten Zip Code Recognition. *Neural Comput.* **1989**, *1*, 541–551. [[CrossRef](#)]
40. Lehmann, E.L.; Casella, G. *Theory of Point Estimation*, 2nd ed.; Springer Texts in Statistics; Springer: New York, NY, USA; Berlin/Heidelberg, Germany, 2005. [[CrossRef](#)]
41. Pu, Z.; Cabrera, D.; Li, C.; de Oliveira, J.V. VGAN: Generalizing MSE GAN and WGAN-GP for Robot Fault Diagnosis. *IEEE Intell. Syst.* **2022**, *37*, 65–75. [[CrossRef](#)]
42. Terven, J.; Cordova-Esparza, D.M.; Ramirez-Pedraza, A.; Chavez-Urbiola, E.A.; Romero-Gonzalez, J.A. Loss Functions and Metrics in Deep Learning. *arXiv* **2023**, arXiv:2307.02694. [[CrossRef](#)]
43. Tzeng, E.; Hoffman, J.; Saenko, K.; Darrell, T. Adversarial Discriminative Domain Adaptation. *arXiv* **2017**, arXiv:1702.05464. [[CrossRef](#)]
44. Easthope, E. (Un)paired signal-to-signal translation with 1D conditional GANs. *arXiv* **2024**, arXiv:2403.04800.
45. Harms, J.; Lei, Y.; Wang, T.; Zhang, R.; Zhou, J.; Tang, X.; Curran, W.J.; Liu, T.; Yang, X. Paired cycle-GAN-based image correction for quantitative cone-beam computed tomography. *Med. Phys.* **2019**, *46*, 3998–4009. [[CrossRef](#)]
46. Chang, B.; Zhang, Q.; Pan, S.; Meng, L. Generating Handwritten Chinese Characters Using CycleGAN. In Proceedings of the 2018 IEEE Winter Conference on Applications of Computer Vision (WACV), Lake Tahoe, NV, USA, 12–15 March 2018; pp. 199–207. [[CrossRef](#)]

47. Zeng, J.; Chen, Q.; Liu, Y.; Wang, M.; Yao, Y. StrokeGAN: Reducing Mode Collapse in Chinese Font Generation via Stroke Encoding. *arXiv* **2021**, arXiv:2012.08687. [[CrossRef](#)]
48. Liu, X.; Liu, S.; Xiang, J.; Sun, R. A transfer learning strategy based on numerical simulation driving 1D Cycle-GAN for bearing fault diagnosis. *Inf. Sci.* **2023**, *642*, 119175. [[CrossRef](#)]
49. He, K.; Zhang, X.; Ren, S.; Sun, J. Deep Residual Learning for Image Recognition. *arXiv* **2015**, arXiv:1512.03385. [[CrossRef](#)]
50. Vaswani, A.; Shazeer, N.; Parmar, N.; Uszkoreit, J.; Jones, L.; Gomez, A.N.; Kaiser, L.; Polosukhin, I. Attention is All you Need. *arXiv* **2017**, arXiv:1706.03762. [[CrossRef](#)]
51. Che, X.; Zhang, H.K.; Li, Z.B.; Wang, Y.; Sun, Q.; Luo, D.; Wang, H. Linearly Interpolating Missing Values in Time Series Helps Little for Land Cover Classification Using Recurrent or Attention Networks. *ISPRS J. Photogramm. Remote Sens.* **2024**, *212*, 73–95. [[CrossRef](#)]
52. Pires, D.S.; Serra, G.L. Methodology for Modeling Fuzzy Kalman Filters of Minimum Realization from Evolving Clustering of Experimental Data. *ISA Trans.* **2020**, *105*, 1–23. [[CrossRef](#)]
53. Choi, J.H.; Jang, S.K.; Cho, W.H.; Moon, S.; Kim, H. Motor PHM on Edge Computing with Anomaly Detection and Fault Severity Estimation through Compressed Data Using PCA and Autoencoder. *Mach. Learn. Knowl. Extr.* **2024**, *6*, 1466–1483. [[CrossRef](#)]

**Disclaimer/Publisher’s Note:** The statements, opinions and data contained in all publications are solely those of the individual author(s) and contributor(s) and not of MDPI and/or the editor(s). MDPI and/or the editor(s) disclaim responsibility for any injury to people or property resulting from any ideas, methods, instructions or products referred to in the content.